AFRL-RX-WP-TP-2008-4330

RELAXATION OF SHOT-PEENED RESIDUAL STRESSES UNDER CREEP LOADING (PREPRINT)

Dennis J. Buchanan, Reji John, and Robert A. Brockman

Metals Branch
Metals, Ceramics, and NDE Division

OCTOBER 2008

Approved for public release; distribution unlimited.

See additional restrictions described on inside pages

STINFO COPY

AIR FORCE RESEARCH LABORATORY
MATERIALS AND MANUFACTURING DIRECTORATE
WRIGHT-PATTERSON AIR FORCE BASE, OH 45433-7750
AIR FORCE MATERIEL COMMAND
UNITED STATES AIR FORCE

REPORT DOCUMENTATION PAGE

Form Approved
OMB No. 0704-0188

The public reporting burden for this collection of information is estimated to average 1 hour per response, including the time for reviewing instructions, searching existing data sources, searching existing data sources, gathering and maintaining the data needed, and completing and reviewing the collection of information. Send comments regarding this burden estimate or any other aspect of this collection of information, including suggestions for reducing this burden, to Department of Defense, Washington Headquarters Services, Directorate for Information Operations and Reports (0704-0188), 1215 Jefferson Davis Highway, Suite 1204, Arlington, VA 22202-4302. Respondents should be aware that notwithstanding any other provision of law, no person shall be subject to any penalty for failing to comply with a collection of information if it does not display a currently valid OMB control number. **PLEASE DO NOT RETURN YOUR FORM TO THE ABOVE ADDRESS**.

1. REPORT DATE *(DD-MM-YY)* October 2008	**2. REPORT TYPE** Journal Article Preprint	**3. DATES COVERED *(From - To)***

4. TITLE AND SUBTITLE
RELAXATION OF SHOT-PEENED RESIDUAL STRESSES UNDER CREEP LOADING (PREPRINT)

5a. CONTRACT NUMBER
In-house

5b. GRANT NUMBER

5c. PROGRAM ELEMENT NUMBER
62102F

6. AUTHOR(S)
Dennis J. Buchanan and Robert A. Brockman (University of Dayton Research Institute)
Reji John (AFRL/RXLMN)

5d. PROJECT NUMBER
4347

5e. TASK NUMBER
RG

5f. WORK UNIT NUMBER
M02R3000

7. PERFORMING ORGANIZATION NAME(S) AND ADDRESS(ES)

University of Dayton Research Institute

Metals Branch (AFRL/RXLMN)
Metals, Ceramics, and NDE Division
Materials and Manufacturing Directorate
Wright-Patterson Air Force Base, OH 45433-7750
Air Force Materiel Command, United States Air Force

8. PERFORMING ORGANIZATION REPORT NUMBER
AFRL-RX-WP-TP-2008-4330

9. SPONSORING/MONITORING AGENCY NAME(S) AND ADDRESS(ES)
Air Force Research Laboratory
Materials and Manufacturing Directorate
Wright-Patterson Air Force Base, OH 45433-7750
Air Force Materiel Command
United States Air Force

10. SPONSORING/MONITORING AGENCY ACRONYM(S)
AFRL/RXLMN

11. SPONSORING/MONITORING AGENCY REPORT NUMBER(S)
AFRL-RX-WP-TP-2008-4330

12. DISTRIBUTION/AVAILABILITY STATEMENT
Approved for public release; distribution unlimited.

13. SUPPLEMENTARY NOTES
Journal article submitted to the ASME Journal of Engineering Materials and Technology.

PAO Case Number: 88ABW 2008-0713; Clearance Date: 28 Oct 2008. The U.S. Government is joint author of this work and has the right to use, modify, reproduce, release, perform, display, or disclose the work. Paper contains color.

14. ABSTRACT
Shot peening is a commonly used surface treatment process that imparts compressive residual stresses into the surface of metal components. Compressive residual stresses retard initiation and growth of fatigue cracks. During the component loading history, loading, or during elevated temperature static loading, such as thermal exposure and creep. In these instances, taking full credit for compressive residual stresses would result in a methodical approach for characterizing and modeling residual stress relaxation under elevated temperature loading, near and above the monotonic yield strength of IN100. The model incorporates the dominant creep deformation mechanism, coupling between the creep and plasticity models, and effects of prior plastic strain. The initial room temperature residual stress and plastic strain profiles provide the initial conditions for relaxation predictions using the coupled creep-plasticity model. Model predictions correlate well with experimental results on shot-peened dogbone specimens subject to single cycle and creep loading conditions at elevated temperature.

15. SUBJECT TERMS
nickel-base superalloy, creep rate, shot peen, residual stress

16. SECURITY CLASSIFICATION OF:			**17. LIMITATION OF ABSTRACT:**	**18. NUMBER OF PAGES**	**19a. NAME OF RESPONSIBLE PERSON** (Monitor)
a. REPORT	**b. ABSTRACT**	**c. THIS PAGE**	SAR	40	James M. Larsen
Unclassified	Unclassified	Unclassified			**19b. TELEPHONE NUMBER** *(Include Area Code)* N/A

Standard Form 298 (Rev. 8-98)
Prescribed by ANSI Std. Z39-18

Relaxation of Shot-Peened Residual Stresses under Creep Loading

Dennis J. Buchanan*, Reji John, and Robert A. Brockman*
Materials and Manufacturing Directorate, Air Force Research Laboratory
(AFRL/RXLMN), Wright-Patterson Air Force Base, OH 45433-7817
*University of Dayton Research Institute, Dayton, OH 45469-0020

Abstract

Shot peening is a commonly used surface treatment process that imparts compressive residual stresses into the surface of metal components. Compressive residual stresses retard initiation and growth of fatigue cracks. During the component loading history, the shot-peened residual stresses may change due to thermal exposure, creep, and cyclic loading. In these instances, taking full credit for compressive residual stresses would result in a nonconservative life prediction. This paper describes a methodical approach for characterizing and modeling residual stress relaxation under elevated temperature loading, near and above the monotonic yield strength of IN100. The model incorporates the dominant creep deformation mechanism, coupling between the creep and plasticity models, and effects of prior plastic strain. The initial room temperature residual stress and plastic strain profiles provide the initial conditions for relaxation predictions using the coupled creep-plasticity model. Model predictions correlate well with experimental results on shot-peened dogbone specimens subject to single cycle and creep loading conditions at elevated temperature. The predictions accurately capture both the shape and magnitude of the retained residual stress profile.

Keywords: Nickel-base superalloy; Creep rate; Shot peen; Residual stress

Introduction

Many metallurgical advances have been achieved in chemistry, melting, and processing techniques to improve the bulk physical, thermal, and mechanical properties of metals. In addition, surface treatments such as shot peening (SP), low plasticity burnishing (LPB) and laser shock peening (LSP) have been employed to enhance damage tolerance by imparting compressive surface residual stresses at fracture-critical locations [1-6]. Compressive residual stresses retard crack initiation and growth, resulting in improved fatigue performance. Numerous studies [3-16] on steels, titanium and nickel-base superalloys have shown that surface treatment induced residual stresses relax when subjected to elevated temperature exposure or mechanical loading. A variety of sophisticated empirical models have been developed and shown to capture trends in residual stress relaxation [12-14]. However, material microstructure, hardening behavior, plastic strain, and the underlying physical deformation mechanisms responsible for stress relaxation are not incorporated into many of these models. This requires that the relaxation model must be recalibrated for each surface treatment process and associated control parameters. As a result, designers lack the confidence to include the beneficial effects of compressive surface residual stresses into fatigue crack initiation or crack growth life prediction codes for fracture-critical locations on turbine engine components.

Surface treatment processes such as SP, LSP, and LPB produce three important changes in the surface treated layers of the material: (1) hardening of the material, i.e., raising the yield strength; (2) large biaxial compressive surface residual stresses constrained by small compensatory tensile stresses distributed through the bulk of the body, and (3) an unstable dislocation structure. The surface treatment deformation results in plastic strain, yield surface, and residual stress profiles that change as a function of depth from the surface. Most residual stress relaxation models in the literature only account for item (2), the initial state of residual stress in the structure. Unfortunately, surface treatment produces a highly deformed and stressed dislocation structure that is easily perturbed by thermal exposure or mechanical loading. Items (1) and (3) must also be incorporated into the models so that residual stress relaxation of other surface treatment processes, such as LSP and LPB, can be included in a deformation mechanism based approach.

Both cyclic and sustained loads may drive relaxation of residual stresses. Room temperature inelastic cyclic loading produces cyclic plastic deformation that changes the residual stress state with repeated cycles. At moderate temperatures and elastic loading conditions, residual stresses are stable with repeated cycles and sustained loading. Sustained elastic loading at elevated temperature produces time-dependent deformation (creep) that changes the residual stress state over time. The synergism between cyclic plasticity and creep deformation mechanisms at elevated temperature is complex. In many cases, multiple deformation mechanisms may be active and contribute to the overall deformation rate. For severe loading conditions or extended long-term exposure, the microstructure may change, resulting in a path- and time-dependent degradation of material properties. Therefore, constitutive models that incorporate evolution equations for the state of the microstructure are essential for capturing the relaxation of residual stresses at elevated temperature.

Creep Deformation Mechanisms and Models

Creep deformation mechanisms in metals may be grouped into a number of broad categories depending on the author [17,18]. Under low stress and high temperature conditions bulk diffusion through the lattice (Nabarro-Herring Creep) dominates, while for low stress and moderate temperatures diffusion along grain boundaries (Coble Creep) becomes the dominant deformation mechanism. At higher stresses and low to moderate temperatures, less than 0.3 T_m (T_m = melting temperature), deformation is controlled by dislocation glide. For temperatures above 0.3 T_m, the mobility of vacancies allows dislocations to climb out of the current glide plane to one of less resistance, thereby increasing the creep rate. Finally, for stresses that reach the theoretical or ideal strength of the crystal, approximately equal to G/30, the material becomes unstable and fractures.

Ranges of stress, temperature, and grain size over which they dominate separate the different deformation mechanisms. Ashby [18] first displayed these graphically on Cartesian maps for a number of pure metals. The abscissas of these graphs are T_h (T_h = homologous temperature), while the ordinates are the normalized tensile (σ/E) or shear stress (τ/G). In some cases, the normalized grain size (d/b) may be the ordinate or third axis for a deformation mechanism cube.

The primary variables associated with creep deformation and creep rate are stress, temperature and time. Much of the early work characterizing creep behavior was aimed at fitting empirical equations as a function of stress, temperature, and time. Furthermore, it is typically assumed that the equations are products separable into functions for stress and temperature. For variable stress and temperature loading conditions a rate formulation must be adopted. The creep strain rate equation is often cast in either a time hardening,

$$\dot{\varepsilon}_c = F_1(\sigma)F_2(T)F_3(t) \tag{1}$$

or, a strain hardening formulation:

$$\dot{\varepsilon}_c = F_1(\sigma)F_2(T)F_4(\varepsilon_c) \tag{2}$$

Both formulations are state variable approaches that may be applied to complex thermal and mechanical loading histories. The time hardening formulation is somewhat cumbersome to implement in that the origin in time must be reset for each stress increment. The strain hardening approach has the additional advantage that time is not included as an independent variable in the model. For these reasons, most creep analyses implement a strain hardening formulation.

A major element missing from the above creep models is the evolution of material microstructure with time or deformation history. It is often assumed that the microstructure and hence the material properties remain unchanged throughout the deformation history. Aspects of the material microstructure such as grain size, dislocation structure, inclusions, vacancies, etc. all have an impact on the deformation rate. Both the time hardening and strain hardening approaches are suitable if the creep rate is dominated by a single deformation mechanism. If multiple deformation mechanisms are active, or the dominant mechanism changes with thermal and mechanical loading history, simple time and strain hardening approaches fail to capture the loading response. Schoeck [17] presents a more general formulation for creep rate that accounts for multiple independent creep mechanisms in the form

$$\dot{\varepsilon}_c = \sum_i f_i(\sigma, T, st)e^{-U_i(\sigma,T,st)/kT} \tag{5}$$

where

f_i = creep rate function (i.e., creep mechanism),

U_i = activation energy for creep mechanism,

σ = applied stress,

T = temperature,

k = Boltzman's constant,

st = structure of the material.

This formulation addresses the evolution of a changing microstructure as a contributing factor to the creep rate, but implies the deformation mechanisms are independent. Numerous models have been developed for the dominant creep mechanisms such as glide and climb of dislocations, and diffusion through grains and along grain boundaries. Nowick and Machlin [19] and Weertman [20] developed the early dislocation creep models to describe climb and glide deformation mechanisms which gave rise to many of the commonly used exponential and hyperbolic sine formulations for creep rate. Interaction or competition between deformation mechanisms may become complex. The Bailey-Orowan equation [17] formulates competing strain hardening and recovery mechanisms with steady state creep as a balance between mechanisms. The θ–projection [21] approach describes primary and tertiary creep using exponential forms with secondary or minimum creep rate as an inflection point in between. Initial approaches to represent material degradation under creep loading include the continuum damage mechanics (CDM) approaches of Kachanov [22] and Rabotnov [23] that incorporate a single damage parameter and associated evolution equation. More recently, the simple damage parameters in the CDM approach have been replaced by specific degradation models representing mechanisms such as cavity nucleation and growth, subgrain coarsening, multiplication of mobile dislocations, and thermally and environmentally driven mechanisms [24-27]. A number of modeling approaches have been developed to account for the combined contributions of plasticity and creep [24-26,28-32] deformation. The trend has been to incorporate plasticity and creep into a single unified inelastic model. The unified models have evolved to include complex nonlinear hardening rules to capture the Bauschinger effect, and cyclic hardening or softening. Unfortunately, the microstructural deformation mechanisms behind creep and plastic deformation, which are fundamentally different, have been combined in this approach. The identification of separate deformation mechanisms for plasticity and creep takes a central role when modeling the effects of prestrain on creep response.

Investigations of the effects of prior room temperature prestrain on creep have been performed in copper [33], nickel [34,35] and aluminum [21]. Parker and Wilshire [33] show that tensile prestrain of five to 12.5 percent change both the primary and secondary creep rates, and that the secondary creep rate decreases with increasing levels of prestrain. The experiments were conducted at a temperature of 0.7 T_m, in which dislocation enhanced diffusion is the rate-controlling mechanism. They also conclude that the primary deformation mechanism is independent of the level of prestrain. Davies et al. [34] investigated elevated temperature compressive prestrain of two to eleven percent on creep in pure nickel. In Davies' study the elevated temperature compressive prestrain increases secondary creep rate by an amount which is independent of the level of prestrain. Evans and Wilshire [21], using two aluminum alloys, demonstrated that in one material secondary creep rate increases with increasing levels of prestrain while in another material secondary creep rate decreases with increasing levels of prestrain, for identical temperatures but different stress ranges. They reason that if the primary deformation mechanism is recovery or climb controlled, then increasing levels of prestrain would result in lower secondary creep rates. If the primary deformation mechanism is glide controlled, then increasing levels of prestrain would result in higher secondary creep rates. In all cases, prior prestrain does affect the subsequent creep rate. The experiments indicate that the level of prestrain, the direction (tensile or compressive) and the dominant deformation mechanism all contribute to whether creep rate increases or decreases with increasing levels of prestrain.

Shot Peening and Residual Stresses

Shot peening has been employed for decades to impart compressive residual surface stresses for retardation of crack initiation and crack growth. Numerous studies have characterized the beneficial effects of compressive residual surface stresses on fatigue life for aluminum-, titanium- and nickel-base alloys [1-3,6,9,11-12]. For applications that utilize aluminum and titanium alloys, subjected to moderate temperatures and stresses, residual stresses are assumed to be stable with repeated cyclic stress-controlled loading. In contrast, nickel-base superalloys are typically selected for applications where temperatures may reach 80 percent of the melting temperature, and stresses approach or exceed the monotonic yield strength. At elevated temperatures and high stress loading conditions, inelastic deformation will alter the original residual stress depth profile. Further, changes to the microstructure resulting from shot peening, long term elevated temperature exposure, and deformation history may accelerate the relaxation rate of residual stresses. Understanding the relaxation of residual stresses is necessary to improve the ability to predict fatigue life of shot-peened components. Currently, designers do not account for the beneficial effect of shot peening, which sometimes results in grossly conservative design practices.

Thermal relaxation studies on shot-peened steels [7-9,13], titanium alloys [3] and nickel alloys [3,5,12,16] have demonstrated that relaxation of residual stresses may occur at relatively low temperatures and over short durations. One of the early thermal residual stress relaxation studies of shot-peened tool steels by Diesner [7] demonstrated that temperature and exposure time are the two driving parameters, and that the rate of relaxation could be captured with a Larson-Miller [36] type creep model. Childs [9], using shot-peened 403 stainless steel Almen strips, observed relaxation at temperatures of 150°C, a quarter of the melting temperature, and for exposure times as short as one hour. Hoffman and coworkers [8] recognized that in addition to temperature and exposure time, the state of the material microstructure is itself another parameter that affects relaxation rate of residual stresses. They used a Zener-Wert-Avrami [37] equation to model relaxation with exposure time, temperature and a fitting parameter that corresponded to the relaxation mechanism. Cao and colleagues [12] developed a thermal recovery model based on the decreasing half-width of x-ray diffraction peaks which they attributed to annihilation and reorganization of crystalline defects. The thermal recovery was modeled as a macroscopic recovery strain that was a function of time and temperature. Prevéy [3,4] has characterized thermal relaxation behavior for a number of materials and surface treatment techniques and has concluded that the rate of relaxation is correlated to the degree of cold working. Prevéy [4] claims that laser shock peening (LSP) and low plasticity burnishing (LPB), which are termed low cold work surface treatment processes, are more resistant to thermal relaxation of residual stresses than conventional shot peening. Thermal relaxation measurements made on superalloy material extracted from retired turbine disks were fit with multi-linear regression analysis by Gabb et al. [5]. Analysis of this data indicated that residual stress relaxation increases with temperature, exposure time, and level of initial cold work.

Mechanical and combined thermal and mechanical relaxation of shot peened residual stresses have been studied on steels [9,13,15], titanium alloys [38], and nickel alloys [11-12,14]. Research into relaxation of residual stresses subject to cyclic loading has followed a much different path than thermal relaxation. For thermal relaxation, temperature and exposure time are the primary parameters, while for fatigue the important factors are temperature, maximum and minimum applied stress, loading frequency, hold time, waveform shape and number of applied cycles. Holzapfel et al. [13] describes residual stress relaxation as three different stages; (1) relaxation due to specimen heating, (2) relaxation during the first cycle, and (3) relaxation with the logarithm of cycle count. A similar approach by Cao et al. [12] describes thermomechanical relaxation as a two-stage process, in which the first stage is a shakedown of the initial residual stresses described by a monotonic stress strain law, and a second stage that is slower and is described by a cyclic softening related to the logarithm of the applied cycles. Another approach [10] performs the shakedown analysis using finite elements with a cyclic plasticity model that incorporates kinematic hardening, followed by a scheme to advance the state variables under constant amplitude loading. The above approaches have the advantage of being numerically efficient for large cycle counts. However, since they rely on the shakedown of residual stresses for constant amplitude loading, they are not appropriate for spectrum loading conditions in which periodic overloads in either tension or compression occur throughout the loading history. For complex spectrum loading conditions, a full constitutive model that integrates the solution forward in time is necessary to capture the state of residual stress at each cycle. The most common formulation is the unified theory that incorporates plasticity, creep and recovery into a single viscoplastic model. Chaboche and Jung [14] using a viscoplasticity model, predict residual stress relaxation in surface treated nickel-based superalloys at elevated temperature. The fundamental flaw in the unified models is the assumption that plasticity, creep and recovery can be combined into a single formulation. This approach contradicts experimental evidence that plasticity, creep and recovery are different deformation mechanisms and as such must be modeled separately, but possibly coupled.

Prevéy [3,4] argues that the rate of residual stress relaxation and amount of relaxation is directly correlated to the level of cold work in surface-treated Ti-6Al-4V and IN718. Prevéy's measurements on IN718 made via x-ray diffraction line broadening show that at the surface, LSP and LPB have less than 10 percent cold work, while shot peening cold work approaches 40 percent for similar peak compressive residual stresses [4]. However, shot peening cold work drops to nearly zero at a depth of 100 microns, while LPB becomes nearly zero at 1000 microns, and LSP exhibits approximately two to three percent to a depth of over 1400 microns. Clearly, the depth of plastic strain and not just the surface value contribute to the relaxation of residual stresses induced by surface treatments.

Therefore, a modeling approach that incorporates both the plastic strain (cold work) and the residual stress depth profiles is required to model relaxation of residual stresses for a multitude of surface treatment processes.

Material Description

IN100 is a powder metal (PM) nickel-base superalloy. The nominal chemical composition of IN100 is listed in Table 1. IN100 has a face-centered cubic (FCC) structure with an average grain size of approximately 25μm. In FCC structures such as this IN100 alloy there are aluminum (Al) atoms at the crystal corners and nickel (Ni) in the center of each face of the crystal which make up the Ni_3Al structure. The microstructure is composed of a continuous gamma (γ) matrix, and precipitate cubical gamma prime (γ'). The cubical gamma prime is responsible for the excellent creep resistance of this alloy. The gamma prime is strong and ductile which limits dislocation interaction and movement through the microstructure. Microstructural studies comparing IN100 samples thermally exposed for 300 hours at 704°C with baseline samples (no exposure) reveal no evidence of grain growth, no gamma prime coarsening, and no new phases detected. These same observations are also true for the heavily cold worked surface layers of the shot peened IN100 samples. Additional details about the baseline microstructure are described in the literature [39].

Experimental Investigation

All baseline characterization of tensile, creep and cyclic properties have been performed on a standard servo-hydraulic test system. The heating system consists of two sets of four quartz lamps to provide temperature control along the length of the sample. Four thermocouples on the sample provide feedback for temperature control. Extensometry measurements are made on both sides of the test specimen to verify that specimen bending, and hence stress gradients, induced in the gage section were negligible. Tensile, creep and fatigue tests are started only if the room temperature and elevated temperature modulus values agreed with expected results and the modulus values from the two opposing extensometers are in agreement with each other, indicating no bending in the gage section.

During the course of each test a low-stress (≈ 400MPa) elastic loading cycle are performed at room temperature and at elevated temperature. Fine ranges on the load cell and extensometer are used to accurately measure the elastic modulus during the elastic loading cycles. The elastic loadings are performed multiple times to determine the repeatability of modulus measurements. All tensile tests are performed in displacement control with the control signal generated by a 16-bit D/A converter. The displacement rate in the elastic region ($< \sigma_y$) has been selected such that the strain rate was nominally 1.0e-3 m/m/s. All tests are conducted in laboratory air using a computer controlled servo-hydraulic test system [40]. The monotonic true stress – true stain response for IN100 at two temperatures, 23°C and 650°C, is shown in Figure 1. Although the elastic modulus and ultimate tensile strength are dependent on temperature, the 0.2 percent yield strength and strain to failure are similar for 23°C and 650°C as shown in Figure 1.

Traditionally, creep data for constant temperatures above 0.4 T_m and at constant stress conditions are often shown in a plot similar to Figure 2. The abscissa is time, which starts after the sample has reached the target stress. The ordinates on the left and right sides respectively, are total strain and strain rate. The solid line represents total strain and the dotted line strain rate. The plot has three regions identified as primary, secondary, and tertiary. The creep rate in the primary region decreases until a minimum or steady-state strain rate is reached in the secondary region. The secondary region is defined by a constant or minimum creep rate. Finally, the tertiary region is defined by increasing strain rate until failure. What is not shown in this type of plot is the material response prior to reaching the desired creep stress. In most materials the response is elastic, and only the initial loading strain is plotted on the graph as the first point. However, nickel-base superalloys, and specifically IN100, have been developed to resist creep deformation at temperatures of 0.8 T_m, and stresses near and above the yield strength. Under these conditions, plastic yielding during loading will affect the creep rate and deformation response. Furthermore, if the material is subject to prior plastic strain at room temperature, elevated temperature yielding may be mitigated. A plot of total strain rate versus total strain that includes the initial loading response to the target creep stress at elevated temperature is necessary. This will capture the elastic, plastic, and creep deformation response of the material.

The effect of room temperature plastic prestrain on creep deformation behavior is shown in Figure 3 for an applied stress of 1000 MPa and temperature of 650°C. The zero percent prestrain case is the baseline case for comparison. The deformation history starts by elastic loading at a constant strain rate of 1.0e-3 m/m/s followed by yielding which produces plastic deformation and a increase in the total strain rate until reaching the target stress after which the strain rate drops off during primary creep deformation. The creep strain rate reaches a minimum and then increases transitioning to tertiary creep. The one percent prestrain case exhibits delayed yielding resulting from an increase in the yield surface during prestrain loading. The minus one percent prestrain loading exhibits a lower tensile yield resulting from the Bauschinger effect and supports the need to include a plasticity model with kinematic hardening. Also, the increase in strain rate is more gradual for the compressive prestrain, which is consistent with the more gradual hardening curve described in the previous paragraphs on cyclic hardening. Only for the five percent prestrain test is yielding mitigated upon loading to 1000 MPa. The data also show that any prestrain, tensile or compressive, results in a decrease in the minimum strain rate. The open diamond symbols represent the initial loading strain, and clearly reflect the complex deformation that occurs prior to reaching the target stress for creep. A similar plot displaying the effect of room temperature plastic prestrain on creep behavior at 900 MPa is shown in Figure 4. Again, the minus one percent prestrain loading exhibits a lower tensile yield resulting from the Bauschinger effect. Also, the increase in strain rate is more gradual for the compressive prestrain, which is consistent with a more gradual hardening curve that is often seen with reversed yielding. At 900 MPa both the one percent and five percent prestrain tests do not yield before reaching the target stress. In this case the compressive prestrain increases the minimum creep rate. This is contrary to observations made at 1000 MPa where any prestrain, tensile or compressive, lowers the minimum creep rate. At 800 MPa the effect of room temperature plastic prestrain on creep behavior is negligible as shown in Figure 5. All tests exhibit a similar minimum creep rate regardless of prestrain level. In this case, only the minus one percent prestrain loading exhibits any yielding during loading since 800 MPa is below the virgin yield strength. The one percent prestrain test has not been completed at this stress level, based on the results of the first three tests. These results also indicate no need to investigate creep response at stress levels below 800 MPa.

Coupled Creep-Plasticity Model

The constitutive model developed in this study is based on a rate-independent plasticity model, and a strain hardening creep model that is coupled to the plasticity model through the plastic strain rate and yield surface size. The plasticity model is based on the von Mises effective stress with a nonlinear mixed isotropic-kinematic hardening rule as described by Dodds [41]. The creep model follows the physics-based modeling of dominant deformation mechanisms similar to the approaches of Ashby, Dyson, McLean and others [18,27]. Based on the SEM and TEM observations of the shot peened and thermally exposed microstructure, it has been argued that the microstructure remains stable over the range of temperatures and exposure times in this study. Therefore a microstructural model dominated by a single deformation mechanism is sufficient to model residual stress relaxation behavior. The elastic-plastic-creep model is cast in an implicit integration form suitable as a standard user material subroutine (UMAT) for implementation into ABAQUS/Standard. Details of the physical deformation mechanism, constitutive equations and solution procedure follow.

Identification of the primary creep deformation mechanism is required before development of a model may begin. One approach to determining the dominant mechanism is to fit the minimum creep rate versus stress data to a power law equation and evaluate the exponent of stress (n). Bulk diffusion through the grain (Nabarro-

Herring Creep) and diffusion along grain boundaries (Coble Creep) may be characterized by minimum creep rates that are directly proportional to stress raised to an exponent n = 1. Dislocation mechanisms such as climb and glide typically have a power law exponent that is higher and with a range of n = 3-5. The creep rate data from this study exhibit an exponent of n ≈ 6, and therefore dislocation motion is the primary deformation mechanism for the range of conditions evaluated. Furthermore, the applied stresses of 800-1000 MPa which are at and above yield, and moderate temperature of 650°C (0.58 T_m) suggest that dislocation glide is dominant over dislocation climb which is a lower-stress, higher-temperature mechanism. Therefore, a creep model with dislocation glide as the dominant deformation mechanism is chosen for this alloy and range of operating conditions.

Many of the viscoplastic models in the literature follow similar arguments about microstructural behavior in the development of the constitutive equation. However, unified models [24-26,28-32] that decompose the total strain rate into elastic and inelastic components as shown by

$$\dot{e}_{ij} = \dot{e}_{ij}^{e} + \dot{e}_{ij}^{in} \qquad [6]$$

imply that plastic and creep deformation are one and the same mechanism. Decomposing inelastic behavior into two rate terms enables independent creep and plasticity deformation mechanisms to be incorporated as shown by

$$\dot{e}_{ij} = \dot{e}_{ij}^{e} + \dot{e}_{ij}^{p} + \dot{e}_{ij}^{c} \qquad [7]$$

This approach implies that creep and plasticity are distinct mechanisms. In fact, they are not independent, but are coupled through a backstress tensor and dislocation mobility model which allows the creep strain rate to be dependent on plastic strain rate, plastic strain and the yield surface.

The development of the creep model follows the microstructurally based deformation mechanism approach of Dyson, McLean and colleagues [27]. The basic model is adapted to incorporate the effects of prior plastic strain and coupling to the plasticity model. The 1D effective creep strain rate relation, based on glide of dislocations as the dominant deformation mechanism, is defined such that it is identical to the axial component under uniaxial loading,

$$\dot{\bar{\varepsilon}}^{c} = \dot{\varepsilon}_{o}\left(1 + \bar{\varepsilon}^{dm}\right) sinh\left(\frac{\bar{\sigma}}{\sigma_{\kappa}\kappa}\right) \qquad [8]$$

where

$\dot{\bar{\varepsilon}}^{c}$ = effective creep strain rate,

$\dot{\varepsilon}_{o}$ = creep strain rate parameter,

$\bar{\varepsilon}^{dm}$ = effective mobile dislocation density,

$\overline{\sigma}$ = effective stress,
σ_κ = normalized stress parameter (nondimensional),
κ = size of yield surface.

The microstructural evolution equation for multiplication of mobile dislocations has been modified to incorporate the effect of plastic strain rate as follows:

$$\dot{\bar{\varepsilon}}^{dm} = M\dot{\bar{\varepsilon}}^{p} + N\dot{\bar{\varepsilon}}^{c} \tag{9}$$

Parameters M and N are coefficients that determine the contributions of plastic strain rate and creep rate toward the increase in dislocation mobility, respectively. In the absence of plastic strain, Equation 9 reduces to the damage rate equation described by McLean and Dyson [27].

The backstress rate ($\dot{\alpha}_{ij}$) is decomposed into components representing yield surface translation ($\dot{\alpha}_{ij}^{p}$), creep backstress ($\dot{\alpha}_{ij}^{c}$), and creep recovery ($\dot{\alpha}_{ij}^{r}$),

$$\dot{\alpha}_{ij} = \dot{\alpha}_{ij}^{p} + \dot{\alpha}_{ij}^{c} - \dot{\alpha}_{ij}^{r} \tag{10}$$

The creep backstress evolution equation is adapted from the nonlinear kinematic hardening rule developed by Armstrong and Frederick [42] for plasticity,

$$\dot{\alpha}_{ij}^{c} = \frac{2}{3}C_c\dot{\varepsilon}_{ij}^{c} - \gamma_c\alpha_{ij}^{c}\dot{\bar{\varepsilon}}^{c} \tag{11}$$

with parameters for strain hardening (C_c) and strain softening (γ_c). The recovery evolution model,

$$\dot{\alpha}_{ij}^{r} = C_1\alpha_{ij}^{p}\dot{\bar{\varepsilon}}^{p} \tag{12}$$

is strictly a function of plastic material behavior and is analogous to the strain softening term in Equation 11. Plastic hardening rules follow the approach in Dodds [41] in the form:

$$\dot{\alpha}_{ij}^{p} = \frac{2}{3}H'(1-\beta)\dot{\varepsilon}_{ij}^{p} \tag{13}$$

$$\dot{\kappa} = \beta H'\left(\varepsilon^{p}\right)\dot{\bar{\varepsilon}}^{p} \tag{14}$$

This formulation incorporates the Bauschinger effect with a mixed nonlinear isotropic-kinematic model where β defines the portion of isotropic hardening and H’ is the plastic modulus. Pure isotropic hardening occurs when β = 1 and pure kinematic hardening when β = 0.

As is typical for metals, it is assumed that hydrostatic stresses have negligible effect on yield behavior and that during plastic flow the material is incompressible. This assumption is also taken to be valid for creep deformation [43,44]. Therefore, all constitutive equations have been based on deviatoric forms of the stress and strain tensors as shown below, respectively.

$$s_{ij} = \sigma_{ij} - \frac{\sigma_{kk}}{3}\delta_{ij} \tag{15}$$

$$e_{ij} = \varepsilon_{ij} - \frac{\varepsilon_{kk}}{3}\delta_{ij} \tag{16}$$

The elastic relationship between stress and strain, shown below in deviatoric form, is the basis for integrating the stresses to the end of the time step.

$$\dot{s}_{ij} = 2G\dot{e}^{e}_{ij} \tag{17}$$

Combining the elasticity equation with the additive strain rate, Equation 7, provides an equation for the dependent stresses in terms of the independent strain rates as,

$$\dot{s}_{ij} = 2G\left(\dot{e}_{ij} - \dot{e}^{p}_{ij} - \dot{e}^{c}_{ij}\right) \tag{18}$$

We adopt Prandtl-Reuss flow equations for both plasticity and creep rate, identifying $\dot{\lambda}_p$ and $\dot{\lambda}_c$ as positive scalar quantities representing the different deformation histories,

$$\dot{e}^{p}_{ij} = \dot{\lambda}_p\left(s_{ij} - \alpha^{p}_{ij}\right) \tag{19}$$

$$\dot{e}^{c}_{ij} = \dot{\lambda}_c\left[s_{ij} - \left(\alpha^{p}_{ij} + \alpha^{c}_{ij} - \alpha^{r}_{ij}\right)\right] \tag{20}$$

The effective plastic strain rate, effective creep rate and von Mises effective stress are defined respectively as,

$$\dot{\bar{\varepsilon}}^{p} = \sqrt{\frac{2}{3}\dot{e}^{p}_{ij}\,\dot{e}^{p}_{ij}} \tag{21}$$

$$\dot{\bar{\varepsilon}}^{c} = \sqrt{\frac{2}{3}\dot{e}^{c}_{ij}\,\dot{e}^{c}_{ij}} \tag{22}$$

$$\bar{\sigma} = \sqrt{\frac{3}{2}\left(s_{ij} - \alpha_{ij}\right)\left(s_{ij} - \alpha_{ij}\right)} \tag{23}$$

Integration of the solution forward in time starts by estimating the creep strain increment for the current material point based on the stress state and state variables at the beginning of the step. The predicted creep strain increment is subtracted from the supplied total strain increment to produce an elastic-plastic strain increment. An elastic-plastic solution follows to calculate an effective plastic strain increment and the stresses at the end of the time step, based on the predicted elastic-plastic strain increment. Then a corrected creep strain increment is calculated based on stresses calculated at the midpoint of the step. The corrected creep strain increment is used to calculate an improved prediction for state variables at the end of the step. The correction procedure is repeated until the difference between the predicted and corrected stresses at the end of the step reaches a specified tolerance limit. If more than a specified number of corrections are needed to achieve the tolerance, a request to cut the time step is returned to ABAQUS. The solution for the elastic-plastic portion of the model follows the work of Braisted and Brockman [45] on a rate-dependent implicit model for Ti-6Al-4V. The solution was adapted to a rate-independent nonlinear isotropic-kinematic hardening model described by Dodds [41]. Another formulation of a coupled creep-plasticity model proposed by Ellyin and Xia [46,47] combines plasticity with a simple power law creep equation to model rate dependent behavior and prior plastic strain effects in multiaxial loading conditions.

Validation of Model

The coupled creep-plasticity model described in the previous section has been calibrated using creep data with prior plastic strain as described in the experimental study section. A one dimensional model of the constitutive equation has been developed as an expedient method to determine the constitutive parameters and associated confidence limits. The parameters deduced from tensile, creep and cyclic tests fit to the one dimensional form of the coupled creep-plasticity model have been implemented into the three dimensional finite element material model.

Overall, the coupled creep-plasticity model captures the effects of prior plastic strain, plastic strain during loading, and applied stress level on the creep deformation response. For example, in the simple case of no plastic prestrain and elastic loading (σ = 800 MPa), shown in Figure 6, there is no plastic material response in any part of the deformation history. The deformation history consists of elastic loading to the target stress at a constant strain rate of 1.0e-3m/m/s is followed by a five decade drop in strain rate. In contrast, Figure 7 incorporates both room temperature plastic prestrain (ε_p = 1 %) and plastic strain during elevated temperature loading at a target stress of σ = 1000 MPa. The model captures the delayed yielding during loading resulting from the increase in the yield surface from room temperature prestrain loading and the sharp increase in strain rate associated with yielding under stress controlled loading. Furthermore, the creep response including the minimum creep rate is accurately captured by the model. Finally, Figure 8 exhibits the case when sufficient plastic prestrain (ε_p = 5 %) expands the yield surface to mitigate elevated temperature loading at a target stress of σ = 1000 MPa. Again, the model accurately captures the complex deformation history and coupling between creep and plasticity.

Application of Model

Shot Peened Specimen Geometry

The proposed coupled creep-plasticity model has been shown to be capable of reproducing material responses over complex loading histories in which inelastic prestrain affects the subsequent creep behavior rather dramatically. This section considers the analysis of relaxation of shot peened residual stresses in IN100 subjected to mechanical loading. Model predictions corresponding to residual stress relaxation of shot peened dogbone specimens are presented to demonstrate the effectiveness of the proposed coupled model for problems involving sharp spatial gradients, such as those encountered in shot-peened components.

Characterization of the initial residual stress and plastic strain depth profiles are necessary for accurate prediction of the evolution of stresses and plastic strains under applied thermal and mechanical loading. The accuracy of stress predictions depends on accuracy of the initial conditions, specifically residual stresses and plastic strains. There are numerous variables that affect the residual stress and plastic strain depth profile. Elastic and inelastic material properties of the material itself have a pronounced effect on the resulting residual stresses and plastic strains. For example, machining and surface finishing processes, such as grinding and polishing, performed prior to shot peening all impart residual stresses into the component. The shot peening process itself has many factors that contribute to the variability of imparted residual stresses, including shot size, hardness, coverage and angle, just to mention a few. Figure 9 is a backscatter SEM micrograph of a polished cross section of IN100. The left side of the image is the shot peened surface of the sample. The left 50 μm area shows a distinct change in microstructure resulting from the shot peening-induced deformation. The right side shows the interior, with a typical representation of the microstructure and individual grains. Superimposed over the microstructure are representative residual stress and percent cold work (plastic strain) depth profiles determined by x-ray diffraction (XRD). Above the plot are three stress-strain images that depict how the residual stress, yield point, and plastic strain change with depth from the shot-peened surface.

Identifying the steps involved in specimen machining, shot peening, mechanical testing, XRD and electropolishing, and analysis of the experiments is necessary to develop an integrated research plan. After identifying limiting factors such as material availability, size of test matrix, and experimental and analytical requirements, a rectangular cross section, dogbone geometry was chosen for the shot peening specimen geometry. A large flat shot peened surface is desired to maximize the size of the irradiated region during XRD. A cylindrical geometry of equal cross sectional area would provide a much smaller surface area for XRD measurement, add complexity in measuring stresses on curves surfaces, and make electropolishing and measuring uniform layer removal for depth profiles more difficult. For the flat dogbone geometry an irradiated x-ray region of 3 x 5 mm with nominal grain size of 25 μm provides approximately 30,000 interrogated grains over which to determine an average residual stress. A specimen width of 10 mm in the gage section provides a 3.5 mm border around the uniformly stressed region for residual stresses to decay to zero at the free surface. A specimen thickness of two mm was selected based on guidance from the shot peening vendor and the capacity of the hydraulic grip hardware. Based on residual stress depth profiles on a similar superalloy, IN718 [3,8] and typical shot peening specifications for turbine engine components [1,2], an Almen intensity of 6A has been selected.

Finite Element Model of Shot Peened Specimen Geometry

The flat dogbone specimen geometry described in the previous section has been designed with both experimental and analytical considerations in mind. The large flat surface of the dogbone sample provides a uniform state of stress in the plane of the sample over an area sufficient for averaging XRD measurements as a function of depth into the sample. The steep gradient and shallow depth of the residual stress profile of shot peening requires an element thickness less than five microns at the surface to accurately represent the stress distribution. Therefore a relatively simple and small geometry is desirable, given the required element size. Figure 10 is an illustration of the dogbone specimen, an enlarged view of the gage section, and a core of the gage section that represents the geometry of the finite element model. The actual model exploits symmetry so only a half-thickness geometry is used for the analysis. The dimensions of the finite element geometry are 100 μm x 100 μm x 1 mm. Uniform displacement boundary conditions are enforced on the surface of the model. This is a reasonable assumption given that the tractions applied to the specimen grip section are far from the gage section. Also, the shot-peened layer is a small fraction of the depth (approximately one tenth), and therefore will provide negligible resistance to the bulk of the thickness deforming uniformly.

Validation of Model Predictions

Although the volume of deformed material is small, the presence of the residual stresses is sufficient to affect the deformation response in the test specimens. Validation of the model with residual stresses is shown in the stress versus strain response of Figure 11. The top and bottom figures show the experimental results and model predictions, respectively, from an unpeened cylindrical dogbone specimen and a shot-peened flat dogbone specimen. The model captures the lower yield point in the shot-peened specimen that is observed in the experimental results. Another effect of residual stresses is observed in the creep deformation behavior. Again, the top and bottom figures show the experimental results and model predictions, respectively. In this case the creep deformation of unpeened cylindrical dogbone specimens tested at 800 and 900 MPa are compared with a shot-peened flat dogbone specimen tested at 800 MPa. Both the experimental results and the model predictions show that the shot-peened specimen exhibits more creep deformation for the same externally applied stress. Furthermore, the effect of the residual stress on the creep deformation is bounded by the 900 MPa unpeened results. These results describe the effect of residual stress on the deformation response of the test coupons. Further validation of the coupled creep plasticity model is accomplished by comparing the measured retained residual stress depth profile after loading with model predictions.

Prediction for retained residual stresses for a single mechanical loading cycle is shown in Figure 11. The maximum applied stress of 900 MPa results in yielding during loading. Three specimens, tested at these conditions, are averaged and shown as a solid line representing the mean response with error bars displaying the range of the XRD measurements for both the axial and transverse residual stress profiles. The range in the XRD measurements is greatest in the region where the residual stress profile has the largest value of compressive residual stress. This is expected since the errors in depth measurement, and stress correction for material removal, are greatest in the shallow depth region. The prediction for the residual stress profiles, shown as the thick lines without symbols, capture the residual stress relaxation trend. Surprisingly, the data displays a small tensile surface residual stress. It has been demonstrated in the literature [48] that gross plastic straining of the entire cross section can reverse the residual stress profile, such that tensile residual stresses occur on the surface with compression in the center. Prediction for retained residual stresses under sustained load (creep) loading, for 30 minutes, is shown in Figure 12. The maximum applied stress of 900 MPa results in yielding during loading. The prediction captures the surface residual stress and peak compressive stress. The measured profile displays a sharp point for the peak compressive residual stress, which is possibly an artifact of the XRD data reduction, and hence is not captured in the prediction. For sustained loading of 10 hours, at the same applied maximum stress of 900 MPa, the retained residual stresses are less than that of the 30 minute profile as shown in Figure 13. Again, the experimental data exhibits a sharp peak in the compressive residual profile.

Clearly sustained loading is more detrimental than the load-unloading cycle to retained compressive residual stresses for applied stresses that develop plastic strain during loading. Furthermore, sustained loading continues to relax residual stresses with increasing creep time. Although significant relaxation of compressive residual stresses occurs during creep relative to that of the load-unload cycle, the surface residual stress remains compressive. This is relatively surprising since analysis of the creep strain data for the 10 hour creep test revealed that the specimen was in tertiary creep and close to failure when the test was stopped.

Conclusions

A new coupled creep-plasticity model that incorporates plastic strain and yield surface state variables has been developed, and used successfully for predicting residual stress relaxation in shot-peened IN100. This model reflects the correct dominant deformation mechanism identified for relaxation of shot-peened residual stresses in this alloy and therefore provides the capability to model relaxation of other surface treatment processes such as LSP and LPB. Creep and plasticity are identified and modeled as different deformation mechanisms, coupled through state variables representing the evolution of the microstructure during deformation. This treatment is contrary to unified models that treat plasticity and creep as the same deformation mechanism grouped into a single rate equation. The coupled creep-plasticity approach facilitates incorporation of other creep deformation mechanisms into the model without additional extensive experimental testing and calibration.

Tensile and creep tests have been completed to characterize the baseline IN100 material at room and elevated temperature. Creep tests with prior room temperature prestrain demonstrate the effect plastic strain has on primary and secondary creep rate behavior. The proposed model has been validated and shown to capture the complex deformation history with prior room temperature prestrain. The model successfully captured the effects of residual stress on deformation history and the retained residual stress profile after several different loading histories.

Acknowledgments

This work was performed at the Air Force Research Laboratory, Materials and Manufacturing Directorate (AFRL/RXLMN), Wright-Patterson Air Force Base, OH 45433-7817 under on-site contract number FA8650-04-C-5200. The authors gratefully acknowledge the partial support of Dr. Leo Christodoulou of the Defense Advanced

Research Projects Agency (DARPA) under DARPA order S271 and Dr. Victor Giurgiutiu of the Air Force Office of Scientific Research (AFOSR) under task 2306-6M2AL8.

References

[1] Happ, M. B., Mourer, D. P., and Schmidt, R. L., "Residual stress analysis and LCF test results for peened bolt hole and dovetail configurations," Proceedings of ASM's Conference on Residual Stress – In Design, Process and Materials Selection, Ed. William B. Young, Cincinnati, OH, April 1987, pp. 127-136.

[2] Vukelich, S., Berkley, S., Russ, S., and Bradley, E. F., "Residual stress measurement and its application to achieve predicted full life potential of low cycle fatigue (LCF) engine disks," The 9th International Symposium on Transport Phenomena and Dynamics of Rotating Machinery, Honolulu, Hawaii, February 2002.

[3] Prevéy, P., Hornbach, D., and Mason, P., "Thermal residual stress relaxation and distortion in surface enhanced gas turbine engine components," Proceedings of the 17th Heat Treating Society Conference and Exposition and the 1st International Induction Heat Treating Symposium, Eds. D.L. Milam et.al., ASM Materials Park, OH, 1998, pp. 3-12.

[4] Prevéy, P., "The Effect of Cold Work on the Thermal Stability of Residual Compression in Surface Enhanced IN718," Proceedings of the 20th ASM Materials Solution Conference & Exposition, St. Louis, MO, October 10-12, 2000.

[5] Gabb, T. P., Telesman, J., Kantos, P. T., Bonacuse, P. J., Barrie, R. L., and Hornbach, D. J., "Stress Relaxation in Powder Metallurgy Superalloy Disks," TMS Letters, The Minerals, Metals & Materials Society, 2004.

[6] Ruschau, J., John, R., Thompson, S., and Nicholas, T., "Fatigue Crack Growth Rate Characteristics of Laser Shock Peened Ti-6Al-4V," ASME J. Eng. Mat. and Tech., **121**, July 1999, pp. 321-329.

[7] Diesner, R. W., "The Effect of Elevated Temperature Exposure on Residual Stresses," SAE Technical Paper No. 710285, SAE, 1971.

[8] Hoffman, J., Scholtes, B., Vöhringer, O., and Macherauch, E., "Thermal relaxation of shot peened residual stresses in the differently heat treated plain carbon steel Ck 45," Proceedings of the Third International Conference on Shot Peening, Eds. H. Wohlfahrt, R. Kopp and O. Vöhringer, Garmisch-Partenkirchen (FRG), 1987, pp. 239-247.

[9] Childs, W. H., "The Effect of Elevated Temperature on Shot Peened 403 Stainless Steel," Analytical and Experimental Methods for Residual Stress Effects in Fatigue, ASTM STP 1004, Eds. R. L. Champoux, J. H. Underwood, and J. A. Kapp, American Society for Testing and Materials, Philadelphia, PA. 1988, pp. 21-24.

[10] Lu, J., Flavenot, J. F., and Turbat, A., "Prediction of Residual Stress Relaxation During Fatigue," Mechanical Relaxation of Residual Stresses, ASTM STP 993, Ed. L. Mordfin, American Society for Testing and Materials, Philadelphia, PA, 1988, pp. 75-90.

[11] Landgraf, R. W., and Chernenkoff, R. A., "Residual stress effects on fatigue of surface processed steels," Analytical and Experimental Methods for Residual Stress Effects in Fatigue, ASTM STP 1004, Eds. R. L. Champoux, J. H. Underwood, and J. A. Kapp, American Society for Testing and Materials, Philadelphia, PA, 1988, pp. 1-12.

[12] Cao, W., Khadhraoui, M., Brenier, B., Guédou, J. Y., and Castex, L., "Thermomechanical relaxation of residual stress in shot peened nickel base superalloy," Material Science and Technology, **10**, November 1994, pp. 947-954.

[13] Holzapfel, H., Schulze, V., Vöhringer, O., and Macherauch, E. "Residual stress relaxation in an AISI 4140 steel due to quasistatic and cyclic loading at higher temperatures," Material Science and Engineering A248, 1998, pp. 9-18.

[14] Chaboche, J. L., and Jung, O., "Application of a Kinematic Hardening Viscoplasticity Model with Thresholds to the Residual Stress Relaxation," International Journal of Plasticity, **13(10)**, 1998, pp. 785-807.

[15] Smith D. J., Farrahi, G. H., Zhu, W. X., and McMahon, C. A., "Experimental measurement and finite element simulation of the interaction between residual stresses and mechanical loading," International Journal of Fatigue, **23**, 2001, pp. 293-302.

[16] Buchanan, D. J., John, R., and Ashbaugh, N. E., "Thermal Residual Stress Relaxation in Powder Metal IN100 Superalloy," Journal of ASTM International, **3(5)**, March 2006.

[17] Schoeck, G., "Theories of Creep," in Mechanical Behavior of Materials at Elevated Temperatures, Ed. J. E. Dorn, McGraw-Hill Book Company, Inc., New York, 1961, pp. 79-107.

[18] Ashby, M. F., "A First Report on Deformation-Mechanism Maps," Acta Metallurgica, **20**, July 1972, pp. 887-897.

[19] Nowick, A. S., and Machlin, E. S., "Quantitative Treatment of the Creep of Metals by Dislocation and Rate Process Theories," National Advisory Committee for Aeronautics (NACA), Technical Note No. 1039, April 1946.

[20] Weertman, J., "Theory of Steady-State Creep Based on Dislocation Climb," Journal of Applied Physics, **26(10)**, October 1955, pp. 1213-1217.

[21] Evans, R. W., and Wilshire, B., Creep of Metals and Alloys, The Institute of Metals, London, 1985.

[22] Kachanov, L. M., "Time of the Rupture Process Under Creep Conditions," Izv. Akad. Nauk. SSR, Otd Tekh., Nauk No. 8, 1958, pp. 26-31.

[23] Rabotnov, Y. N., Creep Problems in Structural Members, North Holland, Amsterdam, 1969.

[24] Chaboche, J. L., “Continuum Damage Mechanics: Part I – General Concepts,” Journal of Applied Mechanics, **55**, March 1988, pp. 59-64.

[25] Chaboche, J. L., “Continuum Damage Mechanics: Part II – Damage Growth, Crack Initiation, and Crack Growth,” Journal of Applied Mechanics, **55**, March 1988, pp. 65-72.

[26] Sanders, D. R., “A Comparison of Several Creep Constitutive Theories for the Prediction of Elastic-Plastic-Creep Response and Their Application to Finite Element Analysis,” Ph.D. Thesis, Texas A&M University, 1986.

[27] McLean, M. and Dyson, B. F., “Modeling the Effects of Damage and Microstructural Evolution on the Creep Behavior of Engineering Alloys,” Journal of Engineering Materials and Technology, **122**, July 2000, pp. 273-278.

[28] Bodner, S. R., “Constitutive Equations for Elastic-Visocplastic Strain-Hardening Materials,” Journal of Applied Mechanics, Transactions of the ASME, June 1975, pp. 385-389.

[29] Walker, K., “Research and Development Program for Nonlinear Structural Modeling with Advanced Time-Temperature Dependent Constitutive Relationships,” NASA Contractor Report, NASA-CR-165533, 1981.

[30] Ramaswamy, V. G., “A Constitutive Model for the Inelastic Multiaxial Cyclic Response of a Nickel Base Superalloy René 80,” NASA Contractor Report 3998, 1986.

[31] Robinson, D. N., “A Unified Creep-Plasticity Model for Structural Metals at High Temperature,” ORNL TM-5969, October, 1978.

[32] Miller, A. K., “An Inelastic Constitutive Model for Monotonic, Cyclic, Creep Deformation: Part I – Equations Development and Analytical Procedures; Part II – Applications to Type 304 Stainless Steel,” Trans. ASME Journal of Engineering Materials and Technology, **96**, 1976, pp. 97.

[33] Parker, J. D., and Wilshire, B., “The Effects of Prestrain on the Creep and Fracture Behavior of Polycrystalline Copper,” Material Science and Engineering, **43**, 1980, pp. 271-280.

[34] Davies, P. W., Finniear, T. C., and Wilshire, B., “The Effect of Compressive Prestrain on the Creep and Fracture Properties of Pure Nickel at 500°C,” Journal of the Institute of Metals, **91**, 1963, pp. 289-292.

[35] Burt, H., Elliott, I. C., and Wilshire, B., “Effects of room-temperature prestrain on creep-fracture behavior of Nimonic 105,” Metal Science, **15**, September 1981, pp. 421-424.

[36] Larson, F. R., and Miller, J., “A Time-Temperature Relationship for Rupture and Creep Stresses,” Trans. ASME, **74**, 1952, pp.765-771.

[37] Avrami, M. J., J. Chem. Phys., **7**, 1939, pp.1103-1112.

[38] John, R., Larsen, J. M., Buchanan, D. J., and Ashbaugh, N. E., "Incorporating Residual Stresses in Life Prediction of Turbine Engine Components," Fatigue, 2002.

[39] Li, K., Ashbaugh, N. E., and Rosenberger, A. H., "Crystallographic Initiation of Nickel-Base Superalloy IN100 at RT and 538°C Under Low Cycle Fatigue Conditions," Superalloys 2004, Eds. K. A. Green, T. M. Pollock, H. Harada, T. E. Howson, R. C. Reed, J. J. Schirra, and S. Walston, TMS, 2004, pp. 251-258.

[40] Hartman, G. A., Ashbaugh, N. E., and Buchanan, D. J., "A sampling of mechanical test automation methodologies used in a basic research laboratory," Automation in fatigue and fracture: testing and analysis, ASTM STP 1231, Ed. C. Amzallag, American Society for Testing and Materials, Philadelphia, PA, 1994, pp. 36-50.

[41] Dodds, R. H., "Numerical Techniques for Plasticity Computations in Finite Element Analysis," Computers & Structures, **26(5)**, 1987, pp. 767-779.

[42] Armstrong, P. J., and Frederick C. O., "A Mathematical Representation of the Multiaxial Baushhinger Effect," CEGB Report RD/B/N731, Berkeley Nuclear Laboratories, Berkeley, UK, 1966.

[43] Johnson, A. E., "The Creep of a Normally Isotropic Aluminum Alloy under Combined Stress Systems at Elevated Temperature," Metallurgia, Vol. 40, 1949, pp. 125.

[44] Kennedy, C. R., Harms, W. O., and Douglas, D. A., "Multiaxial Creep Studies on Inconel at 1500°F," J. Basic Eng., **81**, 1959, pp. 599.

[45] Braisted, W. R., and Brockman, R. A., Laser Shock Peening Analytical Development, UDRI-TR-1999-47, August 1999.

[46] Ellyin, F., and Xia, Z., "A Rate-Dependent Inelastic Constitutive Model – Part I: Elastic-Plastic Flow," Journal of Engineering Materials and Technology, Transactions of the ASME, **113**, July 1991, pp. 314-323.

[47] Xia, Z., and Ellyin, F., "A Rate-Dependent Inelastic Constitutive Model – Part II: Creep Deformation Including Prior Plastic Strain Effects," Journal of Engineering Materials and Technology, Transactions of the ASME, **113**, July 1991, pp. 324-328.

[48] Kirk, D., "Effects of Plastic Straining on Residual Stresses Induced by Shot-Peening," Proceedings of the Third International Conference on Shot Peening, Eds. H. Wohlfahrt, R. Kopp and O. Vöhringer, Garmisch-Partenkirchen (FRG), 1987, pp. 213-220.

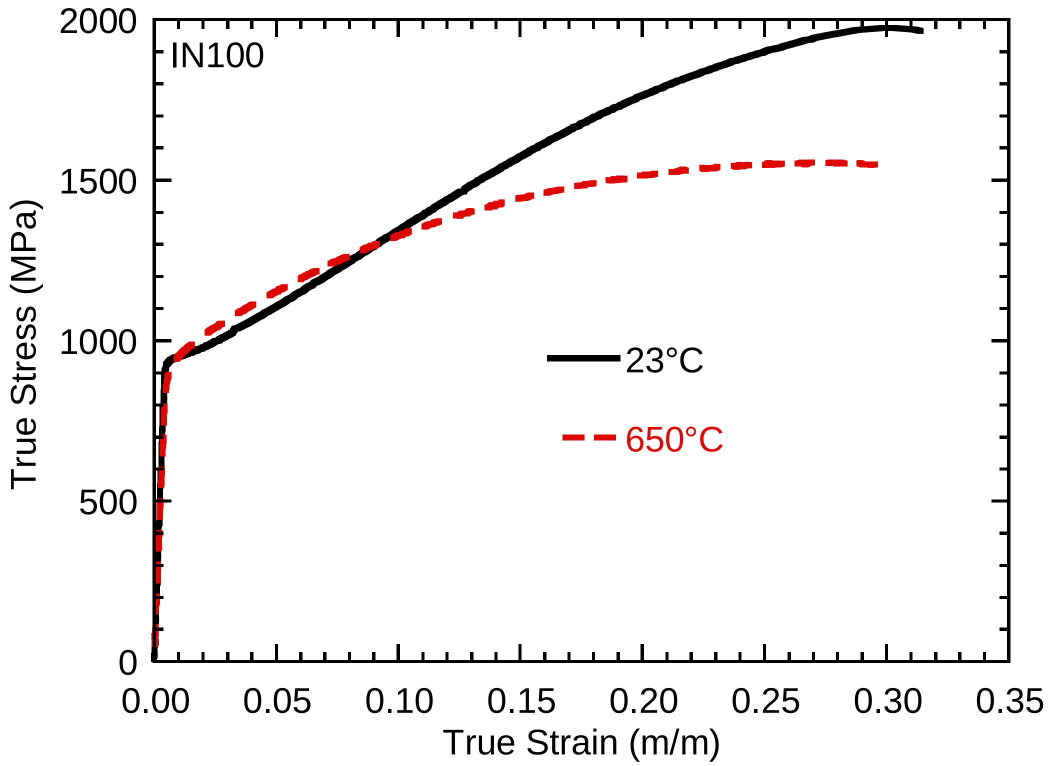

Figure 1. Monotonic true stress versus true strain for IN100 tested at 23°C and 650°C.

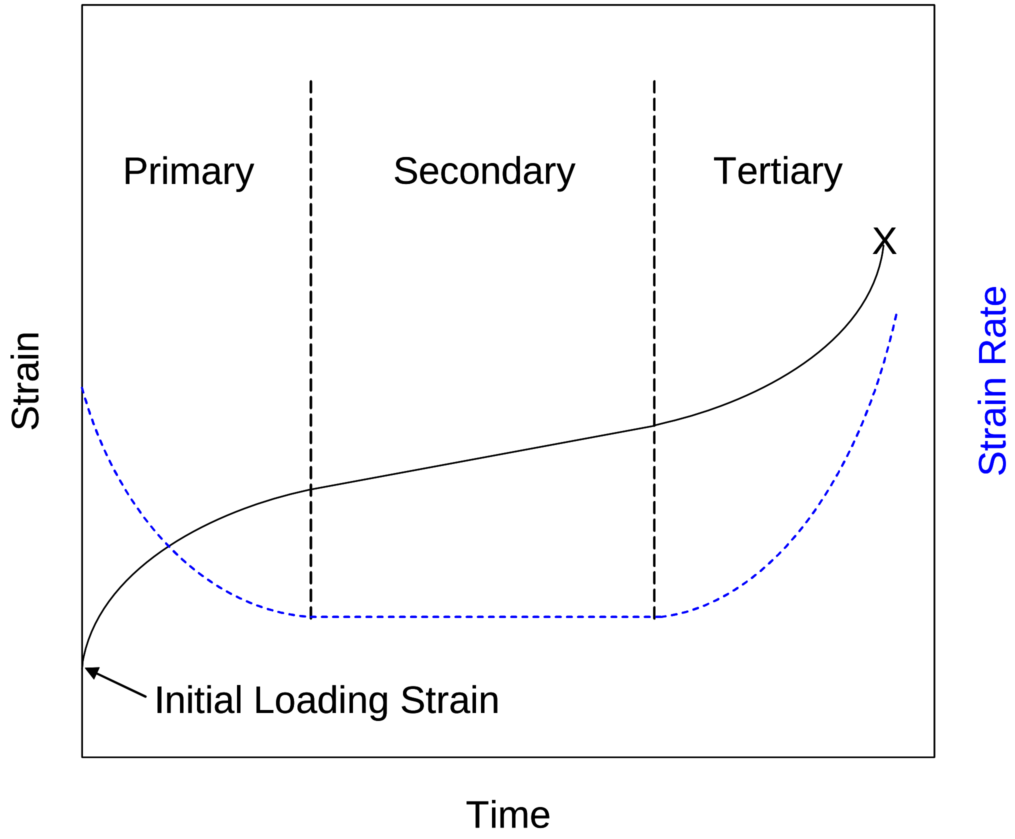

Figure 2. Composite of baseline residual stress and cold work distributions superimposed on shot peened IN100 microstructure.

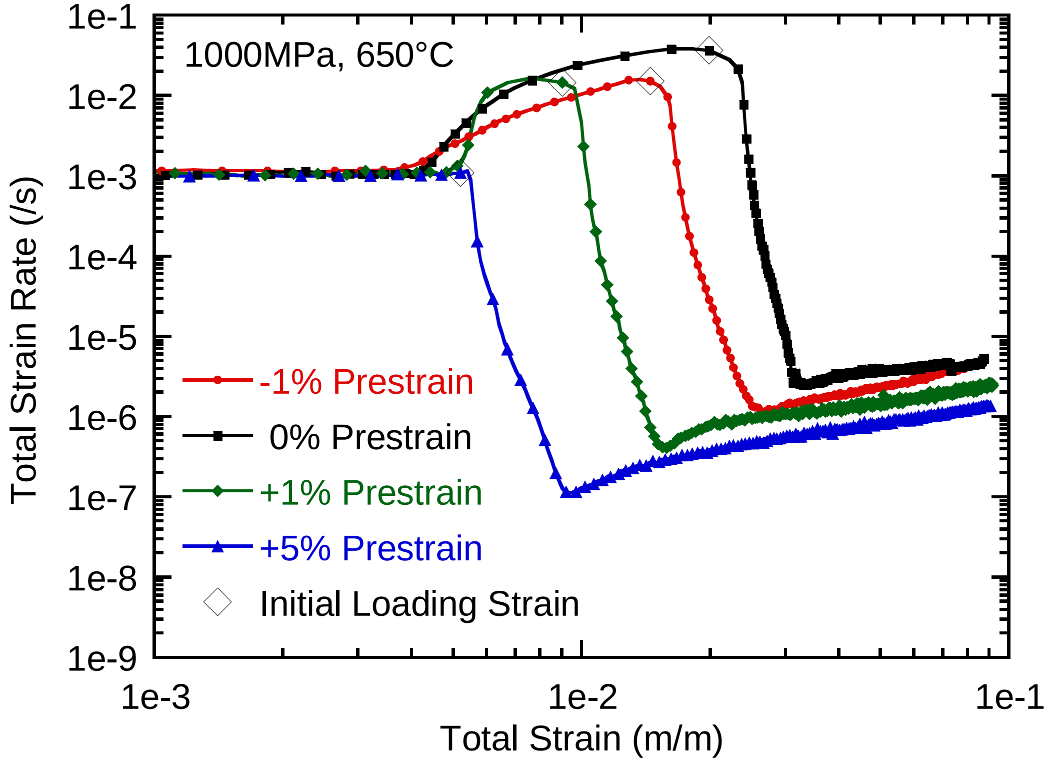

Figure 3. Total Strain Rate versus Total Strain for IN100 at σ_{max} = 1000 MPa and 650°C with Different Levels of Prestrain.

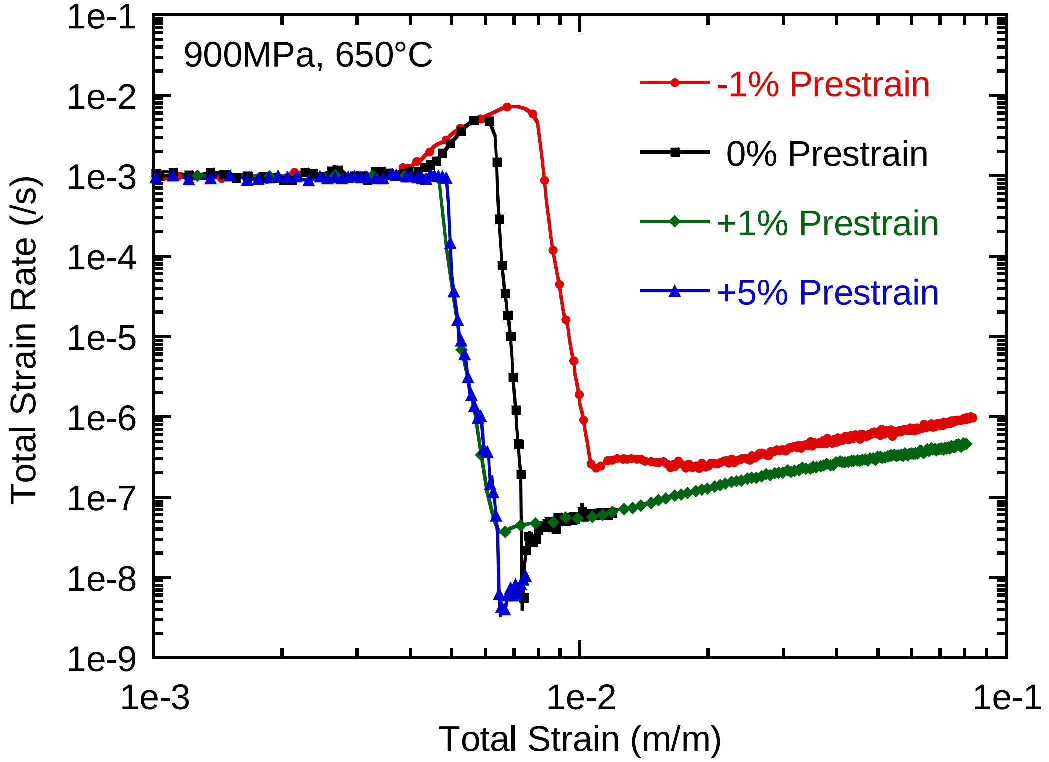

Figure 4. Total Strain Rate versus Total Strain for IN100 at σ_{max} = 900 MPa and 650°C with Different Levels of Prestrain.

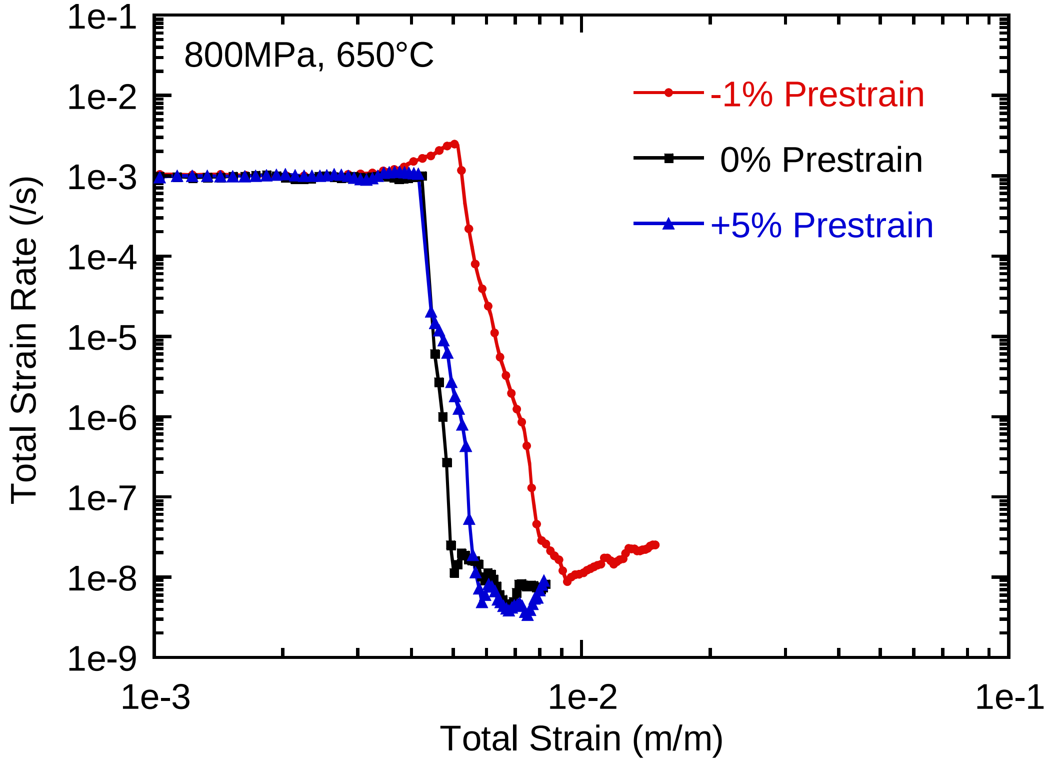

Figure 5. Total Strain Rate versus Total Strain for IN100 at σ_{max} = 800 MPa and 650°C with Different Levels of Prestrain.

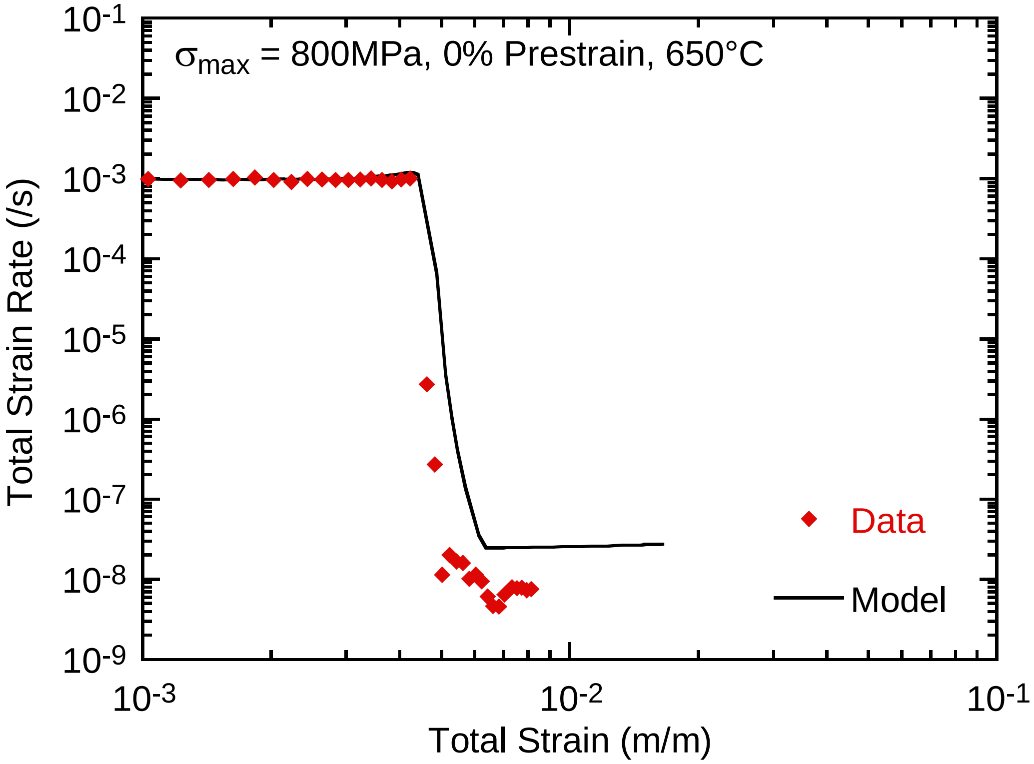

Figure 6. Total Strain Rate versus Total Strain for IN100 at σ_{max} = 800 MPa, 0% RT Prestrain, and 650°C.

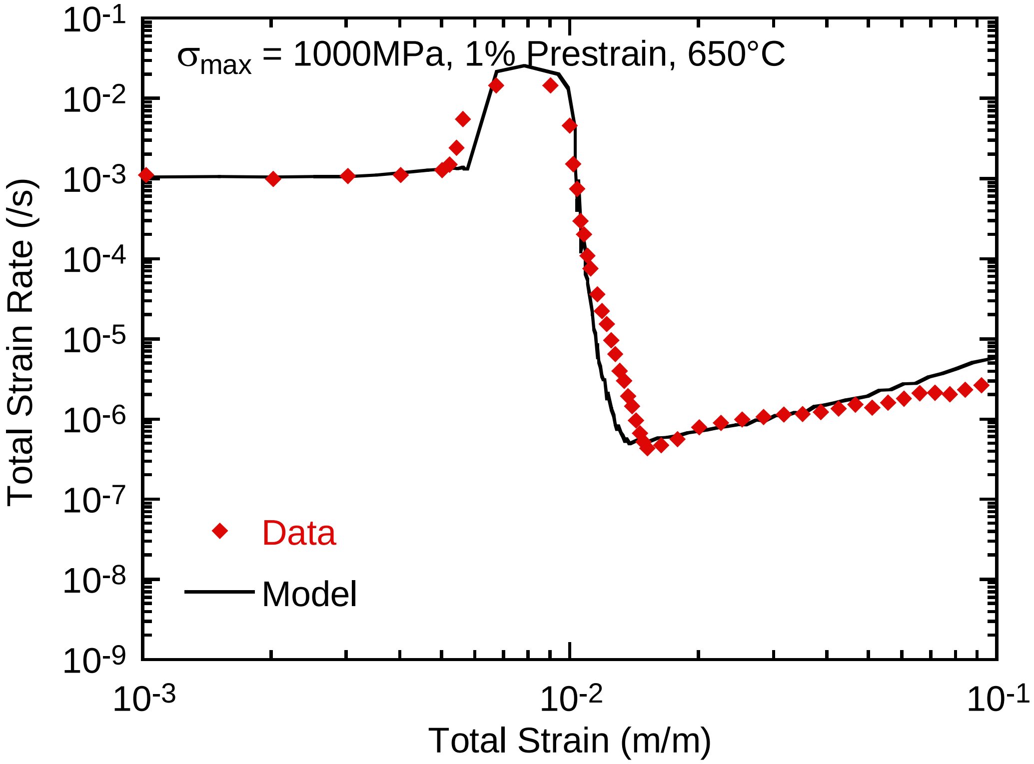

Figure 7. Total Strain Rate versus Total Strain for IN100 at σ_{max} = 1000 MPa, 1% RT Prestrain, and 650°C.

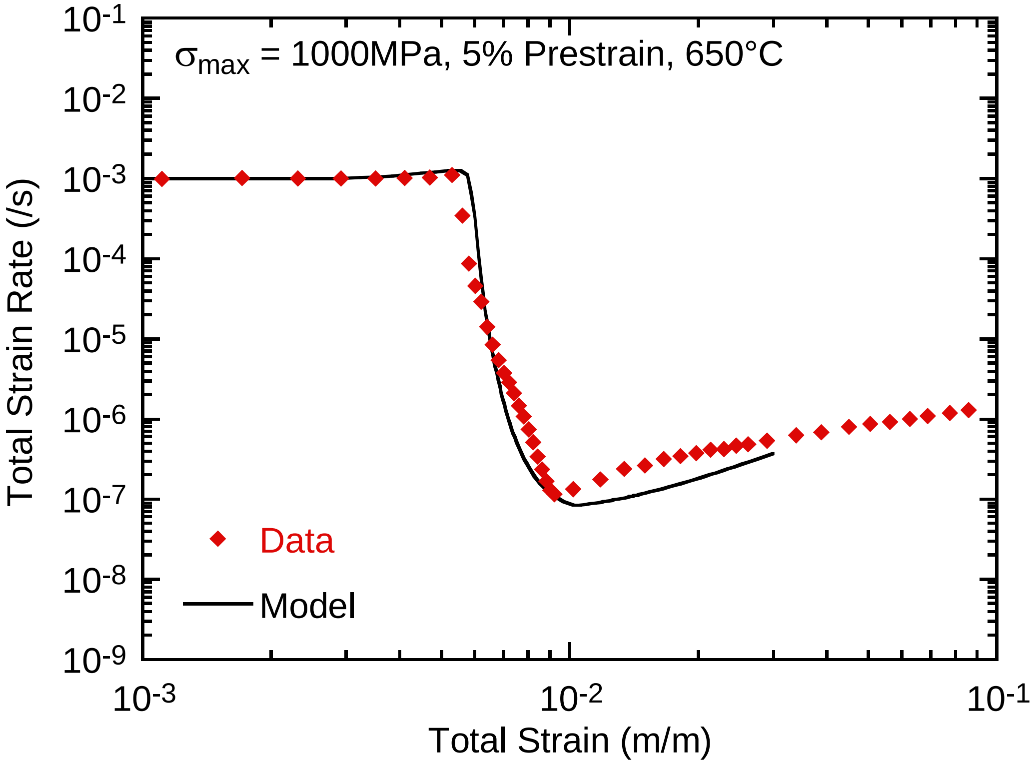

Figure 8. Total Strain Rate versus Total Strain for IN100 at σ_{max} = 1000 MPa, 5% RT Prestrain, and 650°C.

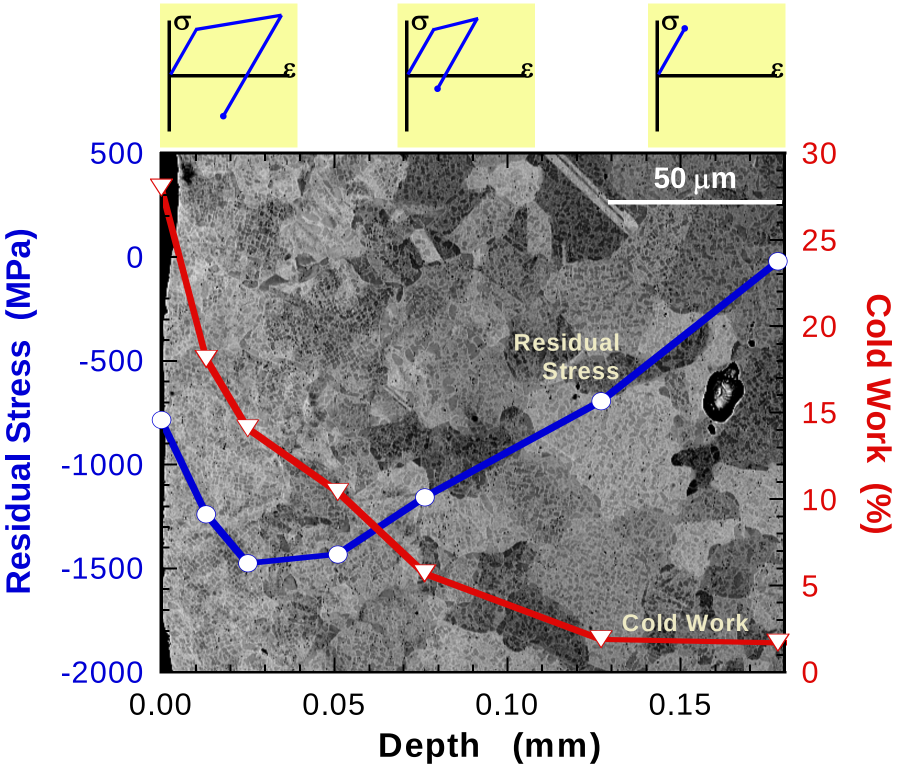

Figure 9. Composite of baseline residual stress and cold work distributions superimposed on shot peened IN100 microstructure.

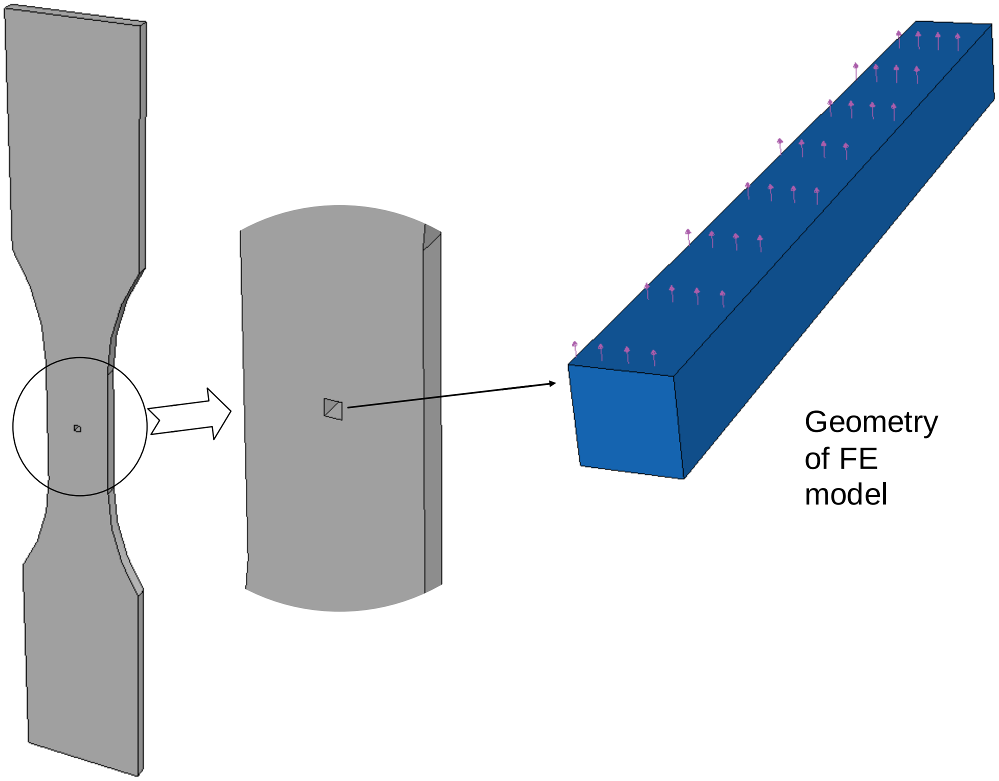

Figure 10. Schematic of dogbone specimen, uniform gage section, and finite element geometry.

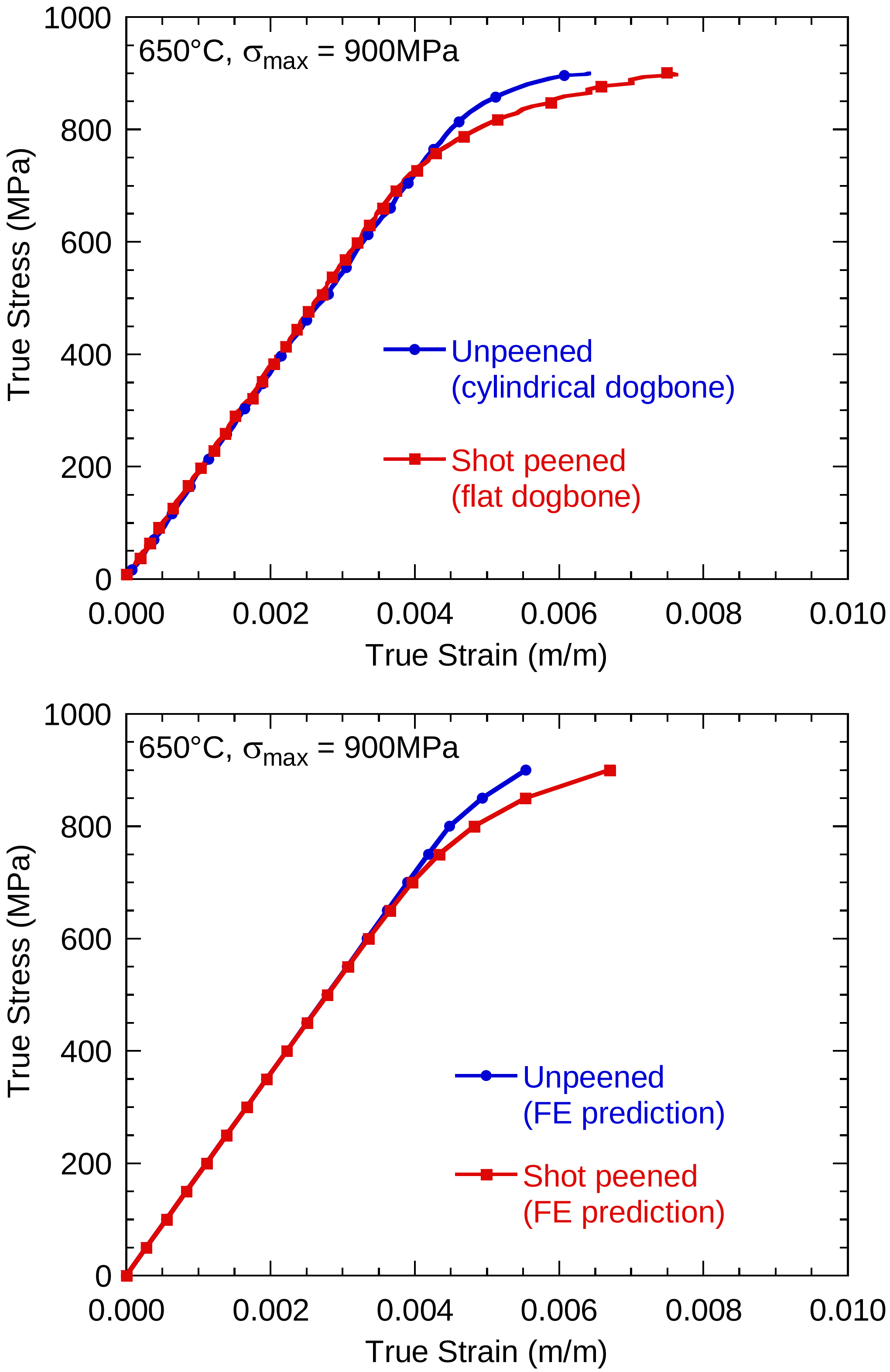

Figure 11. Effect of Shot Peened Residual Stresses on Yielding in IN100 at 900 MPa and 650°C in Virgin and Shot Peened Samples.

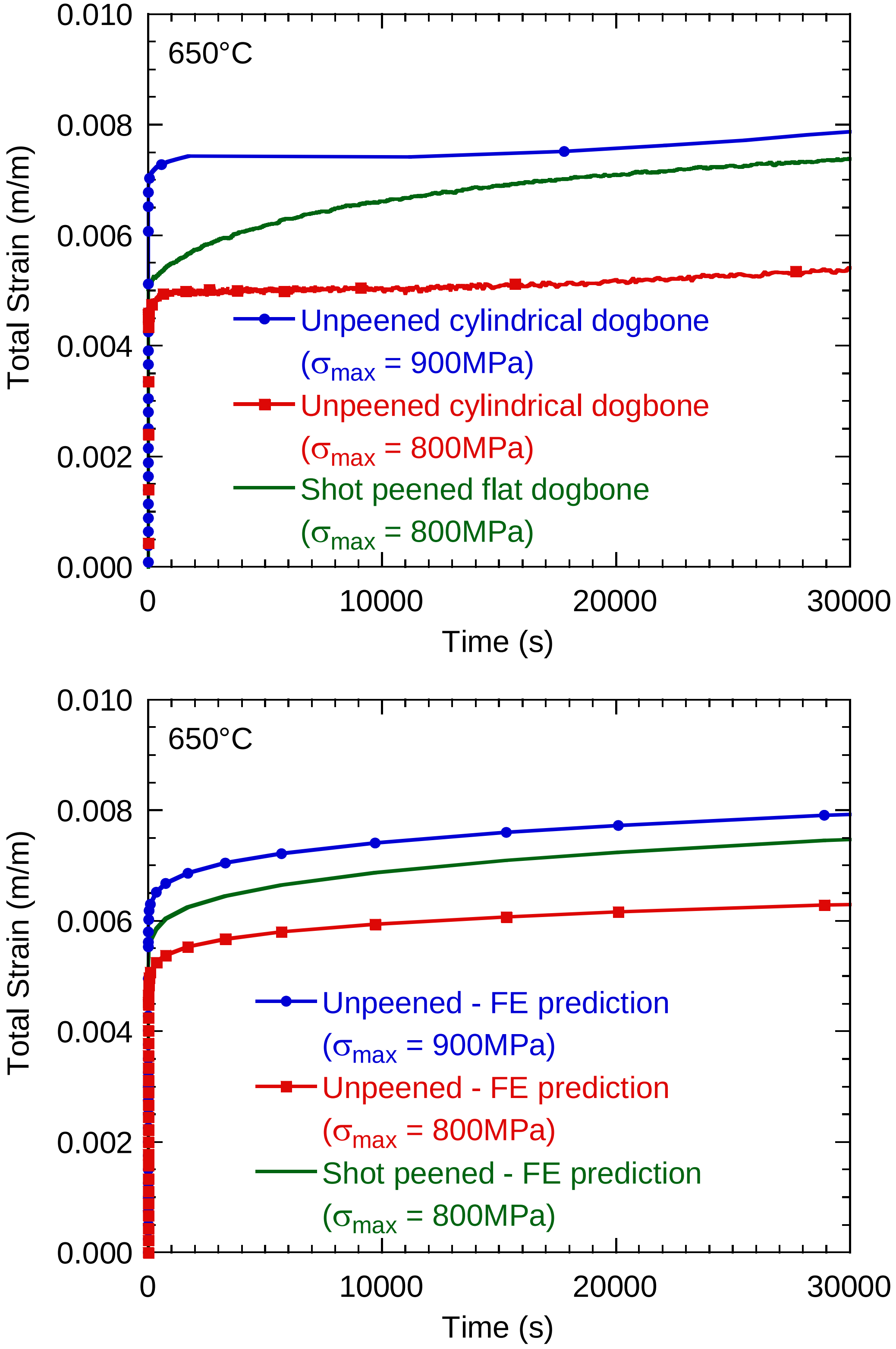

Figure 12. Effect of Residual Stresses on Strain versus Time Response in IN100 at 800 MPa & 900 MPa and 650°C in Virgin and Shot Peened Samples.

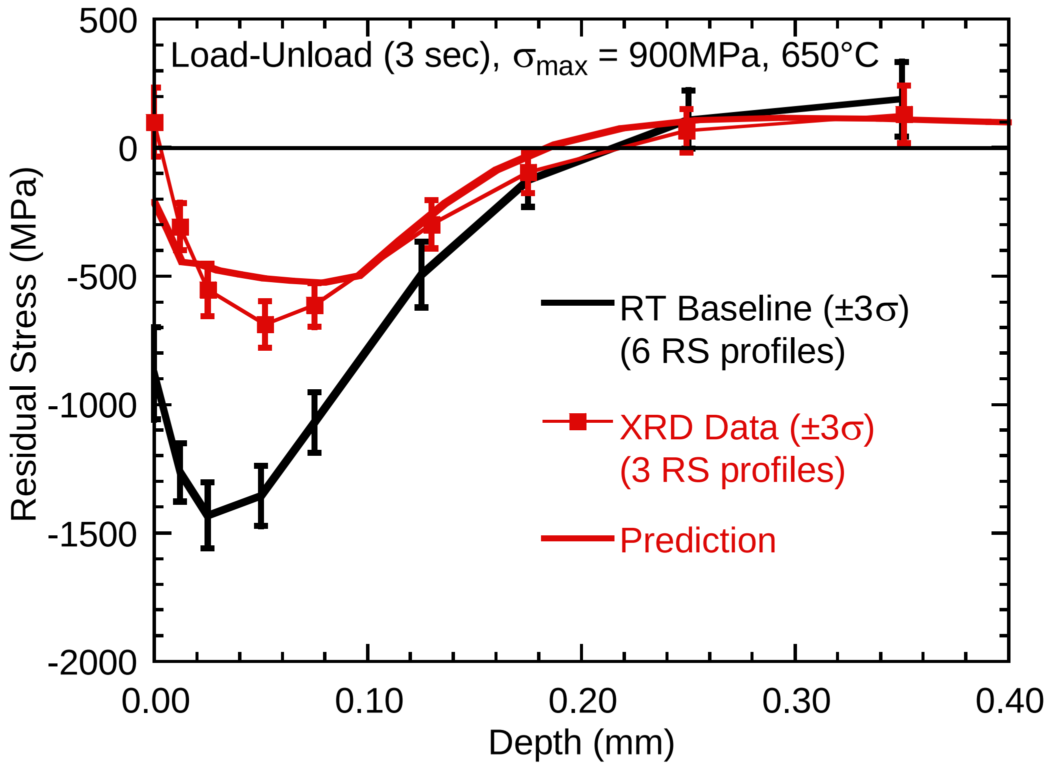

Figure 11. Prediction for Retained Residual Stresses in Shot Peened Dogbone Specimen from Single Load-Unload Cycle in IN100 at 900 MPa and 650°C.

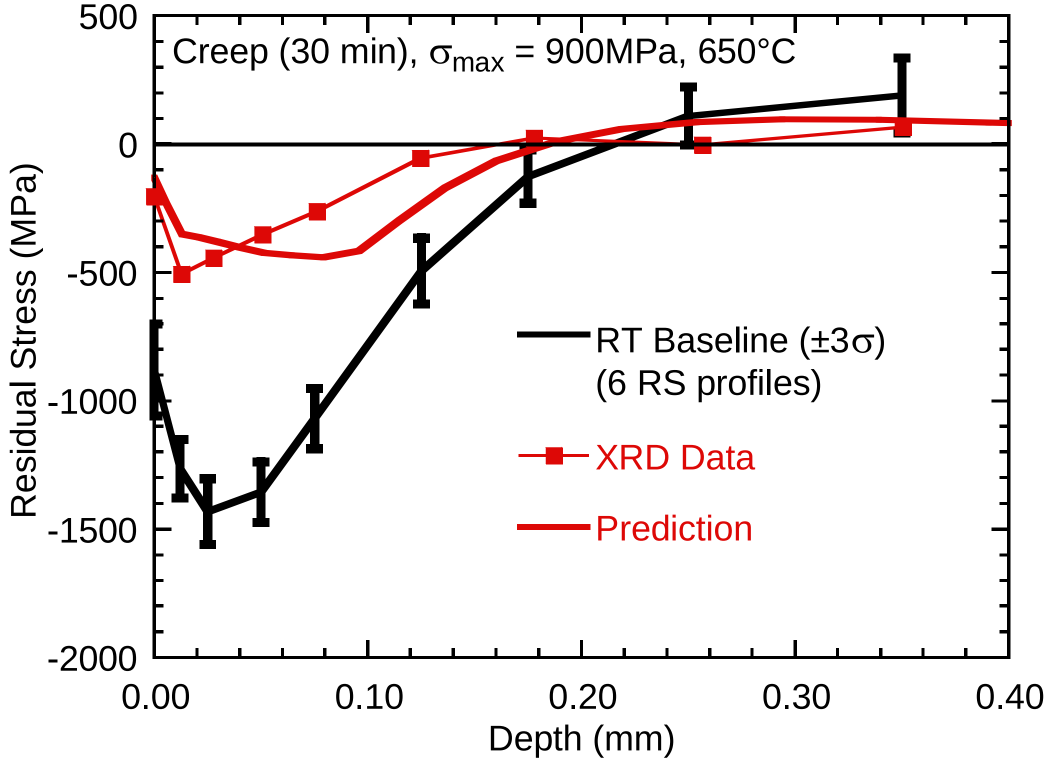

Figure 12. Prediction for Retained Residual Stresses in Shot Peened Dogbone Specimen from 30 min Creep in IN100 at 900 MPa and 650°C.

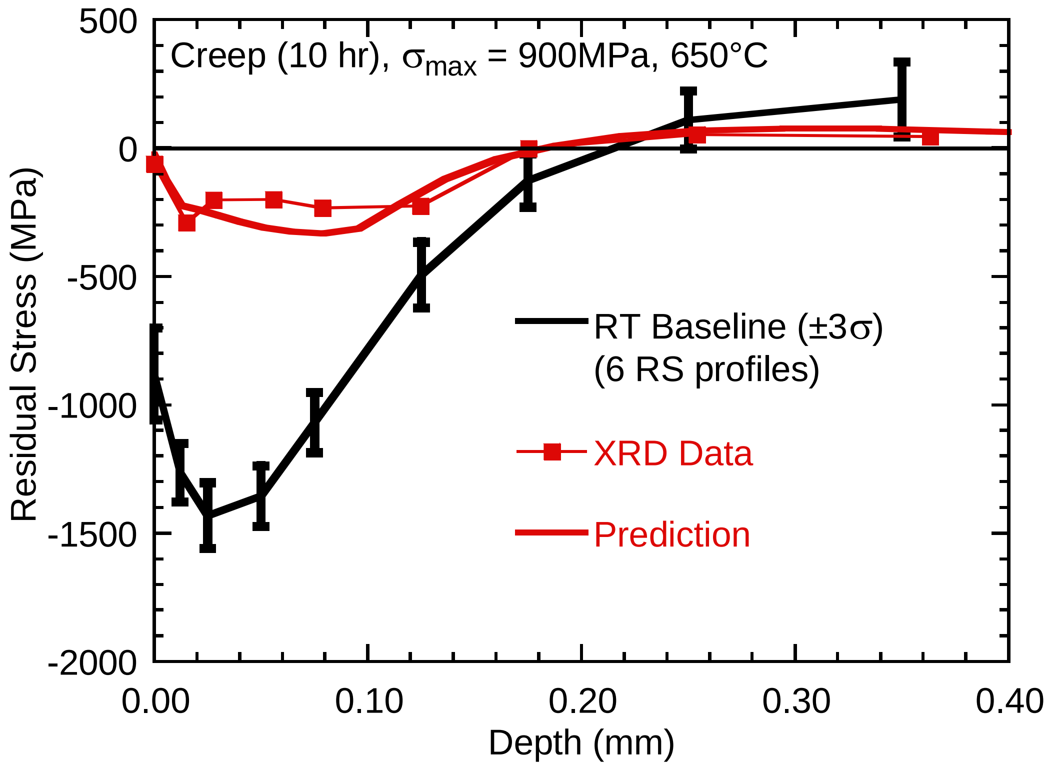

Figure 13. Prediction for Retained Residual Stresses in Shot Peened Dogbone Specimen from 10 hr Creep in IN100 at 900 MPa and 650°C.

Table 1. Chemical Composition of IN100 Nickel-Base Superalloy (wt.%).

Element	**Cr**	**Co**	**Ti**	**Al**	**Mo**	**V**	**C**	**Ni**
Composition	12.4	18.5	4.7	5.5	3.2	0.8	0.07	Bal